LLNL-JRNL-414649

LAWRENCE LIVERMORE NATIONAL LABORATORY

Discovery, Mineral Paragenesis and Origin of Wadalite in Meteorites

H. A. Ishii, A. N. Krot, J. P. Bradley, K. Keil, K. Nagashima, N. Teslich, B. Jacobsen, Q.-Z. Yin

July 13, 2009

American Mineralogist

Discovery, mineral paragenesis and origin of wadalite in meteorites

Hope A. Ishii[1], Alexander N. Krot[2], John P. Bradley[1], Klaus Keil[2], Kazuhide Nagashima[2],
Nick Teslich[1], Benjamin Jacobsen[3], Qing-Zhu Yin[3]

[1] Institute of Geophysics and Planetary Physics, Lawrence Livermore National Laboratory, Livermore, CA 94550, U.S.A.
[2] Hawai‘i Institute of Geophysics and Planetology, School of Ocean and Earth Science and Technology, University of Hawai‘i at Manoa, Honolulu HI 96822, U.S.A.
[3] Department of Geology, University of California at Davis, Davis, CA 95616, U.S.A.
* E-mail of corresponding author: hope.ishii@llnl.gov

Submitting to American Mineralogist

ABSTRACT

The mineral wadalite (ideal and simplified formula: $Ca_6Al_5Si_2O_{16}Cl_3$) has been discovered for the first time in a meteorite, specifically in the coarse-grained, igneous Type B calcium-aluminum-rich inclusions (CAIs) from the CV carbonaceous chondrite Allende. We report the results of electron microprobe, scanning electron microscopy and transmission electron microscopy analyses of wadalite-bearing assemblages in the Allende CAIs and propose that wadalite formed by metamorphic reaction between åkermanitic melilite and anorthite, likely mediated by chlorine-bearing fluids. Petrographic relationships support the likelihood of multistage alterations by fluids of different chemistries interspersed or coinciding with thermal metamorphic episodes on the Allende parent asteroid. Fluid involvement in metamorphism of Allende CAIs implies that these objects experienced open-system alteration after accretion into the CV chondrite parent asteroid which may have resulted in disturbances of their oxygen- and magnesium-isotope systematics.

Keywords: wadalite, Allende, Type B CAIs, aqueous alteration, fluid-mediated metamorphism

INTRODUCTION

Wadalite, a chlorine-bearing, sodium-free mineral, has been identified for the first time in a meteoritic sample – in coarse-grained, igneous calcium-aluminum-rich inclusions (CAIs) from the Allende CV (Vigarano-type) carbonaceous chondrite (Ishii et al. 2008). The ideal wadalite formula is $Ca_6Al_5[O_8(SiO_4)_2Cl_3]$ and typically, it is present in terrestrial occurrences as $Ca_6(Al,Si,Fe,Mg)_7O_{16}Cl_3$. Wadalite is a chlorosilicate belonging to the mayenite-type ($Ca_{12}Al_{14}O_{33}$) family that incorporates excess Cl- and compensates charge via Si^{4+} substitution for Al^{3+}, and it is isometric-hextetrahedral ($\bar{4}3m$) with space group $I\bar{4}3d$ (Tsukimura et al. 1993; Glasser 1995). Chemically, wadalite is similar to grossular ($Ca_3Al_2(SiO_4)_3$), a common secondary mineral found in the Allende CAIs (e.g. Fagan et al. 2007), and to hydrogrossular in which hydroxyl groups replace SiO_4 tetrahedra. Wadalite can be considered a derivative of the hydrogrossular structure, and reaction of hydrogrossular with HCl gas produces wadalite, a chemical reaction of interest in waste management (Fujita et al. 2001 and 2003).

Wadalite was discovered by Tsukimura et al. (1993) in a skarn xenolith in a two-pyroxene andesite from a quarry in Tadano, Koriyama City, Fukushima, Japan. More recently, the mineral has been found in a number of other genetically similar terrestrial occurrences including skarns formed by Tertiary diorite intrusions into Upper Jurassic to Lower Cretaceous limestone at La Negra mine, Queretaro, Mexico, where it is associated with rustumite (a Ca-Cl-silicate), calcite (Ca-carbonate), hydrogrossular and andradite (a Ca-Fe-silicate) and formed as a secondary product of retrogressive hydrothermal alteration of spurrite (a Ca-Si-carbonate) and gehlenite (the Al-rich end-member of the $Ca_2Al_2SiO_7 – Ca_2MgSi_2O_7$ melilite solid solution) (Kanazawa et al. 1997). The mineral has also been found in rocks of the Wiluy River, Yakuia area of Russia, where it occurs with grossular, hydrogrossular and other hydrogarnets (Galuskina and Galuskin 2002); in xenoliths in leucite-tephrite lava from Bellerberg, Germany; and in skarn xenoliths in the

Lakargi Mountain region of the North Caucasus, Russia, where it occurs with calcio-olivine and hillebrandite (both Ca-silicates) (Gobechiya et al. 2008).

Chlorine-bearing minerals in refractory mineral assemblages of CAIs are not generally thought to be primary: CAIs are comprised of the highest temperature condensates predicted to form during cooling of the hot solar nebula and thus not predicted to contain significant volatiles such as chlorine. Instead, alkalis, halogens, Fe, CO_2 and H_2O are commonly attributed to later, secondary alterations (MacPherson et al. 1988, Krot et al. 1995). Precisely how, when and where chlorine was incorporated in CAIs during their lifecycle of formation near the Sun, transport in the nebula, incorporation in meteorite parent bodies, and parent body processing is, however, unclear. Nonetheless, chlorine-bearing minerals in meteorites are of great importance in establishing the abundance and origin of the short-lived radionuclide ^{36}Cl. This, in turns, helps us understand the astrophysical setting for the birthplace of our Solar System. Because of its chlorine-rich (12-13 wt%) and calcium-aluminum-rich composition (~40 wt% CaO and ~20 wt% Al_2O_3), wadalite offers a unique opportunity to study the isotope systematics of three short-lived radionuclides (^{36}Cl-^{36}S with $t_{1/2}$=0.3 Ma, ^{41}Ca-^{41}K with $t_{1/2}$=0.1 Ma, and ^{26}Al-^{26}Mg with $t_{1/2}$=0.73 Ma) (Jacobsen et al. 2009). ^{36}Cl is most likely produced by energetic particle irradiation within the Solar System (Hsu et al. 2006), and measurements in sodalite display variations in $^{36}Cl/^{35}Cl$ initial ratios ranging between $<1.6\times10^{-6}$ and 4×10^{-6} (Lin et al. 2005; Hsu et al. 2006; and Nakashima et al. 2008). The cause of these variations remains ambiguous; Possibilities include heterogeneous distribution of ^{36}Cl in the early Solar System, temporal variations, and disturbance(s) to the ^{36}Cl-^{36}S system in secondary minerals.

We present analyses by electron microprobe, scanning electron microscopy and transmission electron microscopy that confirm the identification of the chlorine-bearing silicate, wadalite, in the Allende meteorite coarse-grained Type B CAIs. (For classification of CAIs, see MacPherson et al. 1988.) Examination of the large- and fine-scale petrography supports involvement of a fluid phase in the formation of meteoritic wadalite and the possibility of multiple alteration episodes on the Allende parent asteroid. Based on these results, we propose a formation mechanism for wadalite in meteoritic settings analogous to that of wadalite in terrestrial settings: metamorphic reaction mediated by fluid.

SAMPLES AND METHODS

Embedded and polished fragments of coarse-grained, igneous (4 Type B and 2 compact Type A) Allende CAIs (Jacobsen et al. 2008) were initially carbon-coated and mapped in Mg, Ca, Al, Na and Cl K_α X-rays using a fully focused electron beam, 15 kV accelerating voltage, 50 nA beam current, 20-30 ms per pixel acquisition time, and resolution of ~2-3 μm per pixel with the wavelength dispersive spectrometer detectors of a Cameca SX-50 electron microprobe at the University of Hawai‘i. In addition to typical secondary minerals, such as nepheline ($Na_3(Na,K)[Al_4Si_4O_{16}]$) and sodalite ($Na_8[Al_6Si_6O_{24}]Cl_2$), replacing melilite and anorthite in the Allende CAIs, sodium-free and chlorine-rich μm-sized grains were identified in all four Type B CAIs studied (Fig. 1). They were subsequently characterized using the JEOL 5900LV scanning electron microscope (SEM) and Cameca SX-50 electron microprobe at the University of Hawai‘i and tentatively identified as wadalite. Detection limits for compositions determined by electron microprobe are 0.02 wt% for MgO; 0.03 wt% for SiO_2, TiO_2, Al_2O_3, and CaO; 0.05 wt% for Na_2O; 0.06 wt% for FeO; and 0.07 wt% for Cl. In a fragment of a Type B CAI AJEF, further secondary and back-scattered electron imaging was carried out using a JEOL JSM-7401F SEM at Lawrence Livermore National Laboratory to locate and prepare regions of interest for extraction and subsequent transmission electron microscopy (TEM) analysis.

Electron transparent thin sections were extracted from wadalite in various petrographic settings in an FEI Nova600 NanoLab dual-beam focused ion beam (FIB) instrument at Lawrence Livermore National Laboratory. The FIB is equipped with a Schottky field emitter electron gun and a liquid gallium ion gun, an Ascend VAXcess *in situ* micromanipulator, and platinum and carbon deposition capabilities. Figure 2 portrays the FIB sample preparation process for one of the sections extracted and analyzed. Secondary electron imaging allows location of the region of interest in the FIB instrument. For this FIB section, prepared for electron diffraction on wadalite, a platinum protective overlayer was deposited by electron and ion beam interaction with a locally injected organometallic gas. The platinum overlayer was positioned over the eventual cross-section to include wadalite boundaries with neighboring minerals. Additional FIB sections were prepared using carbon overlayers deposited in the same manner. The overlayer serves to protect the sample surface from Ga^+ ion beam damage during the subsequent ion milling steps to extract a cross-section, attach it to a TEM half-grid and thin the section to electron transparency.

Imaging, electron diffraction and energy dispersive spectroscopy on FIB-prepared thin sections were carried out in an FEI 200 keV Tecnai TF20 G2 monochromated analytical scanning transmission electron microscope ((S)TEM) with EDAX Genesis 4000 Si(Li) solid state energy-dispersive X-ray detector and a high-resolution Gatan Imaging Filter (GIF) Tridiem. The FIB-deposited, polycrystalline platinum overlayer with d_{111}=2.27Å provided an internal calibration for electron diffraction patterns. Compositions of minerals were determined quantitatively in the STEM using energy dispersive spectroscopy fitting peaks for all elements present in conjunction with a Cliff-Lorimer thin-film correction procedure. Uncertainties depend on collection conditions and, for data presented here, conservative estimates of uncertainty are 0.5 wt% for MgO, 0.7 wt% for Cl, 1.5 wt% for Al_2O_3, 1.0 wt% for SiO_2 and 1.2 wt% for CaO.

RESULTS AND DISCUSSION

Three FIB sections of wadalite from different petrographic settings in the Allende Type B CAI AJEF were prepared and analyzed by TEM. The wadalite mineral identification is presented first followed by the petrographic contexts of wadalite in the CAI and in each FIB section.

WADALITE IDENTIFICATION

Elemental mapping in Allende Type B CAI fragments (Fig. 1), revealed regions rich in chlorine but lacking the correlated sodium expected from sodalite. Table 1 summarizes electron microprobe analyses of these chlorine-bearing grains in Allende.

They show excellent agreement with values reported for terrestrial wadalite (Kanazawa et al. 1997). To confirm this preliminary identification, a FIB section crossing one of these grains was extracted and thinned to electron transparency for TEM analysis (See Figure 2). Figure 3a shows a bright field TEM image of the FIB section, and Figure 3b-c show selected area electron diffraction patterns from the [120] and [110] zones (measured TEM sample holder tilt angle of 18° between zones) confirming the identification of wadalite with a cubic $I\bar{4}3d$ lattice and a_o = 12.0Å in agreement with the original data for the type specimen of Tsukimura et al. (1993). An energy dispersive spectrum in Figure 3d measured by analytical TEM is consistent with the compositions measured by electron microprobe (Table 1).

PETROGRAPHIC CONTEXT

The Allende sample AJEF is a fragment of a coarse-grained, igneous Type B CAI composed of melilite, fassaite, spinel and anorthite. Figure 1a shows a combined elemental map of AJEF in Mg (red), Ca (green) and Al (blue) K_α X-rays, and Figure 1b shows AJEF mapped in Cl (red), Na (green) and Al (blue) K_α X-rays. Both melilite ($Åk_{19-64}$) and fassaite (Al,Ti-diopside with 2-11 wt% TiO_2, 14-18 wt% Al_2O_3) display chemical zoning. Increasing Åk content in melilite is accompanied by Na enrichment as previously reported in Allende CAIs (Hutcheon et al. 1978; Barber et al. 1984). The observed correlation of Åk and Na (Fig. 4) is consistent with igneous partitioning of Na between melilite and liquid during fractional crystallization of the Na-bearing Type B CAI melts (Becket et al. 2000). Melilite is cross-cut by veins composed primarily of fine-grained grossular, monticellite ($CaMgSiO_4$) and forsterite (Fig. 5). Åkermanitic melilite around anorthite and fassaite grains shows more extensive replacement by secondary grossular, monticellite and minor wollastonite (Figs. 5, 6a). Secondary nepheline and sodalite are minor. Alteration regions are ~80-100 μm in width between the melilite and anorthite, wider than those between melilite and fassaite. Also unlike fassaite, anorthite exhibits a coarse, corroded interface with the alteration region (Figs. 5, 6b) suggesting it may have been preferentially dissolved/corroded by a fluid phase.

Wadalite is typically present in regions of fine-grained secondary alteration between anorthite and åkermanitic melilite and commonly occurs with grossular, monticellite and wollastonite. Wadalite is present in the form of distinct grains reaching approximately 15 μm across (Fig. 6b–c) and is also found intergrown in irregular shapes and filling veins in melilite (Fig. 6d). Surveys of additional Allende CAIs have shown wadalite to be common in the interiors of Type B CAIs (Fig. 7) and rare in Compact Type A CAIs.

Two FIB sections were produced crossing grains of wadalite identified by red arrows in Figure 6b. The first cross-section, Wdl1, provided the definitive identification of wadalite (described above) and includes the wadalite grain and neighboring grossular and melilite. The wadalite-grossular boundary (Fig. 3a) has a smooth, equilibrated interface that may reflect gentle metamorphic processing. The wadalite-melilite boundary, in contrast, is much more complex. Figure 8 shows that melilite is present as fine laths rooted in wadalite and extending into void spaces that appear suggestive of vestiges of fluid (or gaseous) inclusions. Interestingly, STEM-EDS traverses in the wadalite grain between the grossular interface and the melilite/void interface show no compositional zoning (5.6 wt% MgO, 17 wt% Al_2O_3, 27 wt% SiO_2), and no crystallographic relationship between wadalite and grossular or wadalite and melilite was found by electron diffraction. A TEM-EDS traverse along one of these melilite laths (Fig. 8a) showed highly localized chemical zoning over a few micron distance from $Åk_{\sim 25}$ at the wadalite interface increasing to $Åk_{\sim 60}$ moving away from the interface. Such strong zoning is indicative of rapidly changing relative availability of Al, Mg and Si during crystallization. The melilite also shows high stacking disorder contrast consistent with relatively rapid formation and little annealing. A lack of corrosional relationship between intergrown wadalite and melilite (Fig. 8b) suggests this melilite could be secondary and co-crystallized with the wadalite. These observations are consistent with alteration of CAI AJEF by a penetrating, mobile medium. Rounded inclusions are also evident in the melilite, especially along grain boundaries and at interfaces with wadalite (Fig. 8c). The larger inclusions, 30–50 nm in diameter, were most likely formed by fluid or gas. The small size of the inclusions has precluded determination of their contents to date.

The second FIB section, Wdl2, crosses a wadalite grain in an alteration region between åkermanitic melilite and anorthite. The section shown in Figure 9a includes the wadalite grain (4.1 wt% MgO, 20 wt% Al_2O_3, 21 wt% SiO_2) bounded by spinel on one side and monticellite plus melilite on the other. Wdl2 reveals a void space formed by termination of the wadalite grain above, grossular below, spinel on one side and monticellite plus melilite on the other. No direct wadalite-grossular interface is present. This large void (~4.5 μm in its longest dimension) is angular and appears to be the result of incomplete volume filling by the surrounding mineral grains which terminate at the void in smooth surfaces. This large void is likely the result of volume change during formation of grossular-bearing assemblages: Reactions between melilite and anorthite generating various grossular-bearing assemblages (Krot et al. 2007)

$$\underset{\text{melilite solid solution}}{(3Ca_2MgSi_2O_7 + Ca_2Al_2SiO_7)} + \underset{\text{anorthite}}{CaAl_2Si_2O_8} = \underset{\text{grossular}}{2Ca_3Al_2Si_3O_{12}} + \underset{\text{monticellite}}{3CaMgSiO_4}$$

$$\underset{\text{melilite solid solution}}{(3Ca_2MgSi_2O_7 + Ca_2Al_2SiO_7)} + \underset{\text{anorthite}}{2CaAl_2Si_2O_8} = \underset{\text{grossular}}{3Ca_3Al_2Si_3O_{12}} + \underset{\text{monticellite}}{CaMgSiO_4} + \underset{\text{forsterite}}{Mg_2SiO_4}$$

$$\underset{\text{melilite solid solution}}{(4Ca_2MgSi_2O_7 + Ca_2Al_2SiO_7)} + \underset{\text{anorthite}}{CaAl_2Si_2O_8} = \underset{\text{grossular}}{2Ca_3Al_2Si_3O_{12}} + \underset{\text{monticellite}}{4CaMgSiO_4} + \underset{\text{wollastonite}}{CaSiO_3}$$

$$\underset{\text{melilite solid solution}}{(Ca_2MgSi_2O_7 + Ca_2Al_2SiO_7)} + \underset{\text{fluid}}{SiO_{2(aq)}} = \underset{\text{grossular}}{Ca_3Al_2Si_3O_{12}} + \underset{\text{monticellite}}{CaMgSiO_4}$$

produce volume changes calculated to be approximately 13–18%. The wadalite-spinel and grossular-spinel mineral interfaces are smooth; however, ~50–100 nm voids are present at the grossular-spinel interface on the grossular side of the interface (Fig. 9b) and in the grossular-monticellite interface. These suggest either fluid or gasses trapped at the interface or volume change during formation. The monticellite is either intimately intergrown with or contains inclusions of melilite ($Åk_{\sim30}$) and titanium-free diopside with two compositions (2 wt% Al_2O_3 and 9 wt% Al_2O_3, both with 0.2 wt% Cr_2O_3).

A third FIB section, Wdl3, crosses a vein of wadalite in melilite. A few-micron-sized void is present in the interface between melilite ($Åk_{\sim43}$) and the secondary minerals filling the vein (Fig. 10a). The melilite bordering this void has a rough surface as if corroded. The secondary minerals are a closely intergrown combination of micron and submicron regions of irregularly shaped crystals of wadalite, monticellite, grossular and (most likely secondary) melilite with numerous small micron-sized and nanometer-sized void spaces interspersed at grain boundaries. Due to over-thinning of the central portion of this FIB section, EDS traverses to test for zoning in the wadalite would be unreliable; however, EDS spectra were collected from wadalite in several locations over the section show compositions slightly more Mg-rich and Al-poor (typically 6.9 wt% MgO, 15 wt% Al_2O_3, 25 wt% SiO_2) than those in the wadalite grains Wdl1 and Wdl2. Wadalite frequently abuts voids (as do the other secondary minerals); however, an apparent inclusion of wadalite is present within a larger region of grossular (Fig. 10b). The fine-grained, intermixed nature of the assemblage of minerals suggests relatively rapid formation, and the petrographic setting in a vein in melilite strongly suggest fluid transport to emplace these secondary alteration minerals. Void spaces may be due to volume change during formation or escape of fluid.

PARAGENESIS AND ORIGIN

Based on the observed petrographic occurrence of wadalite in Allende CAIs, we propose its formation as a result of metamorphic reaction between åkermanitic melilite and anorthite, most likely mediated by fluid, that results in alteration regions consisting of fine-grained assemblages of grossular, monticellite, wollastonite, forsterite and wadalite. The presence of wadalite in alteration regions and emplaced in veins in melilite suggests that a chlorine-bearing, possibly siliceous fluid was present during or following the thermal metamorphism that generated grossular-bearing assemblages at modest temperatures inferred for the Allende parent body (Meeker et al. 1983; Barber et al. 1984; Krot et al. 1998a,b; Zolotov et al. 2006; Zolotov and Mironenko 2007; Ford and Brearley 2007; Krot et al. 2008). Wadalite may have formed simultaneously with its neighboring secondary minerals or by a subsequent fluid alteration via chlorine-bearing fluids of grossular (or hydrogrossular) to which it is closely chemically related. Veins in melilite containing secondary anorthite and grossular but lacking any sodium- or chlorine-bearing minerals (Fig. 11) indicate that there were likely multiple episodes of fluid alteration involving different chemical compositions. Wadalite intimately intergrown with grossular, monticellite, wollastonite and (likely secondary) melilite in a vein in melilite may also be due to alteration postdating earlier generation metamorphism and alteration that generated and relocated the grossular, monticellite and wollastonite in this vein since there are sufficient void spaces intersecting wadalite to have permitted fluid infiltration. Alternatively, wadalite may have formed concurrently with the grossular-bearing assemblages. In either case, the lack of hydrous phases in these Allende CAIs indicates that moderate thermal metamorphism postdated fluid alteration(s) (Krot et al. 1998a,b; Zolotov et al. 2006).

Observations by SEM and (S)TEM suggest that wadalite grains crystallized more slowly – at least initially – giving rise to larger crystal sizes and more regular interfaces with neighboring mineral phases. Wadalite and accompanying minerals in veins likely formed more rapidly producing smaller crystal sizes and irregular, intimate intergrowths and may be the result of later alterations in which earlier generation alteration minerals were corroded or dissolved and reformed. The wadalite-melilite interface in Wdl1 is an interesting case: The large wadalite grain displays no measurable chemical zoning and a smooth and equilibrated interface with grossular, but the melilite shows strong, highly localized zoning and is present as fine laths suggesting this melilite is secondary and formed in dynamic conditions. In addition, there appears to be evidence for co-crystallized wadalite and melilite. Again, the secondary melilite and co-crystallized wadalite may be the result of a later fluid incursion and metamorphic episode.

What is not clear in the case of Allende CAIs is how significant metasomatism via fluid transport may have been. In terrestrial settings, wadalite forms in skarns by hydrothermal alteration (e.g. Kanazawa et al. 1997) with considerable mass and chemical transport implicated in the process. Calcium loss, which is seen in the Allende CAI AJEF, has been shown to result from alteration and exchange processes that typically also produce nepheline and sodalite (Krot et al. 1998b). The source of chlorine in wadalite is uncertain at present: it may have been captured in condensed ices (c.f. Zolotov and Mironenko 2007), condensed or reacted in fine-grained volatile-rich matrices originally accreted on the parent body, or dissolved in silicate melts (Bridges et al. 1997). The observed differences in abundances of chlorine-bearing phases between the oxidized Allende-like and reduced CV3 chondrites suggest that chlorine was mobile and redistributed during alteration (Krot et al. 1998b).

Involvement of a fluid phase in the formation of wadalite, as petrography indicates, requires that some of the alterations of Allende CAIs occurred on the parent body asteroid rather than prior to accretion of the asteroid in the solar nebula. In this case, there is a strong possibility of chemical – and isotope – exchange on the asteroid parent body, and Allende CAIs likely did not behave as closed systems. Isotope exchange on the parent body may explain some of the oxygen-isotope heterogeneities observed in melilite and anorthite (e.g. Ito et al. 2004; Krot et al. 2008) as well as the disturbance of ^{26}Al-^{26}Mg systematics in Allende CAIs (Hutcheon et al. 1978).

Acknowledgements

We thank Herbert Palme for providing several Allende CAI fragments including AJEF and A39 used in this study and Steve Simon and Larry Grossman for additional Allende CAIs. Portions of this work were performed under the auspices of the U.S. Department of Energy by Lawrence Livermore National Laboratory in part under contract No. W-7405-Eng-48 and in part under contract DE-AC52-07NA27344. This work was supported by NASA Grants NNX08AE08G to KK, NNH06AF991 to JPB, and NNH09AK26I to HAI. QZY acknowledges support of an IGPP Minigrant from LLNL and NASA grants NNX08AG57G and NNX09AC93G.

References

Barber, D.J., Martin, P.M and Hutcheon, I.D. (1984) The microstructure of minerals in coarse-grained Ca-Al-rich inclusions from the Allende meteorite. Geochimica et Cosmochimica Acta, 48, 769-783.

Beckett, J.R., Simon, S.B. and Stolper, E. (2000) The partitioning of Na between melilite and liquid: Part I. Application to Type B inclusions from carbonaceous chondrites. Geochimica et Cosmochimica Acta, 64, 2519-2534.

Bridges, J.C., Alexander, C.M.O'D., Hutchison, R., Franchi, I.A. and Pillinger, C.T. (1997) Na-, Cl-rich mesostases in Chainpur (LL3) and Parnalee (LL3) chondrules. Meteoritics, 32, 555-556.

Fagan, T.J., Guan, Y. and MacPherson, G.J. (2007) Al-Mg isotopic evidence for episodic alteration of Ca-Al-rich inclusions from Allende. Geochimica et Cosmochimica Acta, 42, 1221-1240.

Ford, R. and Brearley, A.J. (2007) Phyllosilicates in two coarse-grained Allende CAIs: Evidence for advanced hydration. Proceedings of the 38th Lunar and Planetary Science Conference, abstract 2411, Lunar and Planetary Institute, Houston, Texas.

Fujita, S., Suzuki, K., Ohkawa, M., Shibasaki, Y. and Mori, T. (2001) Reaction of hydrogrossular with hydrogen chloride gas at high temperature. Chemistry of Materials, 13, 2523-2527.

Fujita, S., Suzuki, K., Mori, T. and Shibasaki, Y. (2003) A new technique to remove hydrogen chloride gas at high temperatures using hydrogrossular. Industrial and Engineering Chemistry Research, 42, 1023-1027.

Galuskin, E. and Galuskina, I. (2002) Achtarandite – sponge hibschite pseudomorph after wadalite-like phase: internal morphology and mechanism of formation. Neues Jahrbuch für Mineralogie – Abhandlungen, 178, 63-74.

Glasser, F.P. (1995) Comments on wadalite, $Ca_6Al_5SiO_{16}Cl_3$, and the structures of garnet, mayenite and calcium chlorosilicate. Addendum. Acta Crystallographica, C51, 340.

Gobechiya, E.R., Yamnova, N.A., Zadov, A.E. and Gazeev, V.M. (2008) Calcio-olivine γ-Ca_2SiO_4: I. Rietveld refinement of the crystal structure. Crystallography Reports, 53, 404-408.

Hsu, W., Guan, Y., Leshin, L.A., Ushikubo, T., and Wasserburg, G.J. (2006) A late episode of irradiation in the early solar system: Evidence from extinct ^{36}Cl and ^{26}Al in meteorites. Astrophysical Journal, 640, 525-529.

Hutcheon, I.D., Steele, I.M., Smith, J.V. and Clayton, R.N. (1978) Ion microprobe, electron microprobe and cathodoluminescence data for Allende inclusions with emphasis on plagioclase chemistry. Proceedings of the 9th Lunar Planetary Science Conference, pp. 1345-1368, Lunar and Planetary Institute, Houston, Texas.

Ishii, H.A., Krot, A.N., Keil, K., Nagashima, K., Bradley, J.P., Teslich, N., Jacobsen, B. and Yin, Q.-Z. (2008) Discovery of wadalite in Allende Type B CAI. Proceedings of the 39th Lunar and Planetary Science Conference, abstract 1989, Lunar and Planetary Institute, Houston, Texas.

Ito, M., Nagasawa, H. and Yurimoto, H. (2004) Oxygen isotopic SIMS analysis in Allende CAI: details of the very early thermal history of the solar system. Geochimica et Cosmochimica Acta, 68, 2905-2923.

Jacobsen, B., Yin, Q.-Z., Moyniera, F., Amelin, Y., Krot, A.N., Nagashima, K., Hutcheon, I.D. and Palme, H. (2008) ^{26}Al-^{26}Mg and ^{207}Pb-^{206}Pb systematics of Allende CAIs: Canonical solar initial $^{26}Al/^{27}Al$ ratio reinstated. Earth and Planetary Science Letters, 272, 353-364.

Jacobsen, B., Matzel, J., Hutcheon, I. D., Ramon, E., Krot, A. N., Ishii, H. A., Nagashima, K. and Yin, Q.-Z. (2009) The ^{36}Cl – ^{36}S systematics of wadalite from the Allende meteorite. Proceedings of the 40th Lunar and Planetary Science Conference, abstract 2553, Lunar and Planetary Institute, Houston, Texas.

Kanazawa, Y., Aoki, M. and Takeda, H. (1997) Wadalite, rustumite, and spurrite from La Negra mine, Queretaro, Mexico. Bulletin of the Geological Survey of Japan, 48, 413-420.

Krot, A.N., Scott E.R.D. and Zolensky M.E. (1995) Mineralogical and chemical modification of components in CV3 chondrites: Nebular or asteroidal processing? Meteoritics, 30, 748-775.

Krot, A.N., Petaev, M.I., Zolensky, M.E., Keil, K. Scott, E.R.D. and Nakamura, K. (1998a) Secondary calcium-iron-rich minerals in the Bali-like and Allende-like oxidized CV3 chondrites and Allende dark inclusions. Meteoritics and Planetary Science, 33, 623-645.

Krot, A.N., Petaev, M.I., Scott, E.R.D., Choi, B.-G., Zolensky, M.E. and Keil, K. (1998b) Progressive alteration in CV3 chondrites: More evidence for asteroidal alteration. Meteoritics and Planetary Science, 33, 1065-1085.

Krot, A.N., Yurimoto, H., Hutcheon, I.D., Libourel, G., Chaussidon, M., Tissandier, L., Petaev, M.I., MacPherson, G.J., Paque-Heather, J. and Wark, D. (2007) Type C Ca, Al-rich inclusions from Allende: Evidence for multistage formation. Geochimica et Cosmochimica Acta, 71, 4342-4364.

Krot, A.N., Chaussidon, M., Yurimoto, H., Sakamoto, N., Nagashima, K., Hutcheon, I.D. and MacPherson, G.J. (2008) Oxygen isotopic compositions of Allende Type C CAIs: Evidence for isotopic exchange during nebular melting and asteroidal metamorphism. Geochimica et Cosmochimica Acta, 72, 2534-2555.

Lin, Y., Guan, Y., Leshin, L.A., Ouyang, Z. and Wang, D. (2005) Short-lived chlorine-36 in a Ca- and Al-rich inclusion from the Ningqiang carbonaceous chondrite. Proceedings of the National Academy of Science, 102, 1306-1311.

MacPherson, G.J., Wark, D.A. and Armstrong J.T. (1988) Primitive material surviving in chondrites: Refractory inclusions. In Meteorites and the Early Solar System, eds. J.F. Kerridge and M.S. Matthews, University of Arizona Press, Tucson, 746-807.

Meeker, G.P., Wasserburg, G.J. and Armstrong, J.T. (1983) Replacement textures in CAI and implications regarding planetary metamorphism. Geochimica et Cosmochimica Acta, 47, 707-721.

Nakashima, D., Ott, U., Hoppe, P., and El Goresy, A. (2008) Search for extinct ^{36}Cl: Vigarano CAIs, the Pink Angel from Allende, and a Ningqiang chondrule. Geochimica et Cosmochimica Acta 72, 6141–6153.

Tsukimura, K., Kanazawa, Y., Mashahiro, A. and Bunno, M. (1993) Structure of wadalite $Ca_6Al_5Si_2O_{16}Cl_3$. Acta Crystallographica, C49, 205-207.

Zolotov, M.Y., Mironenko, M.V. and Shock, E.L. (2006) Thermodynamic constraints on fayalite formation on parent bodies of chondrites. Meteoritics and Planetary Science, 41, 1775-1796.

Zolotov, M.Y. and Mironenko, M.V. (2007) Hydrogen chloride as a source of acid fluids in parent bodies of chondrites. Proceedings of the 38th Lunar and Planetary Science Conference, abstract 2340, Lunar and Planetary Institute, Houston, Texas.

Figure Captions

Figure 1. Focused ion beam (FIB) thin section preparation. (a) Back-scattered electron image collected prior to FIB thin section preparation of a region in AJEF containing wadalite grain Wdl1 (see Fig. 6b–c). (wdl=wadalite, grs=grossular, mel=melilite, mnl=monticellite). Secondary electron images collected in the FIB at 52° tilt showing the same region (b) prior to FIB deposition and milling, (c) following deposition of a platinum overlayer to protect the region to be extracted, (d) during ion milling of trenches on either side of the cross-section and (e) after ion milling of an undercut to partially release the section. (f) An ion image after removal of the section from the substrate, transfer to a TEM half grid and severing of the attachment to the micromanipulator needle.

Figure 2. A brightfield transmission electron microscopy image (a) shows a FIB section (Wdl1) through a wadalite grain bounded by grossular on one side and melilite on the other. Selected area electron diffraction patterns (b, c) along the [120] and [110] zones confirm the identification of wadalite. The polycrystalline platinum (Pt) pattern is inset. An energy-dispersive X-ray spectrum from the wadalite (c) is consistent with compositions measured by electron microprobe (Table 1). Ga is an artifact resulting from focused ion beam milling. (wdl=wadalite, grs=grossular, mel=melilite).

Figure 3. Combined elemental maps of the Allende CAI AJEF (~2 mm across) (a) constructed from Mg (red), Ca (green) and Al (blue) K_α X-rays and (b) constructed from

Cl (red), Na (green) and Al (blue) K_{α} X-rays. Red outlined box in a) indicates region in Figure 6. In b), red regions correspond to wadalite, green regions correspond to nepheline, and yellow regions correspond to sodalite. (an=anorthite, sp=spinel, fas=fassaite, mel=melilite, grs=grossular).

Figure 4. Concentration of Na_2O (wt%) versus åkermanite content (mol%) in melilite in the Allende Type B CAI AJEF.

Figure 5. Back-scattered electron image of the grossular-bearing veins cross-cutting melilite in Allende CAI AJEF (an=anorthite, fas=fassaite, fo=forsterite, grs=grossular, mcl=monticellite, mel=melilite, sp=spinel).

Figure 6. Backscattered electron images of representative regions containing wadalite in Allende CAI AJEF. (a) Åkermanitic melilite around anorthite and fassaite show extensive replacement by alteration products grossular, monticellite and wollastonite. Thicker alteration regions that include wadalite surround anorthite. (b) A higher magnification of the region marked in (a) shows locations of two grains of wadalite (red arrows). Wadalite is commonly found adjacent to melilite, grossular and monticellite. (c) and (d) show two petrographic settings for wadalite. In (c), wadalite is present as a discrete grain, and in (d), wadalite fills a vein in melilite. (an=anorthite, fas=fassaite, mel=melilite, sp=spinel, grs=grossular, mnl=monticellite, wdl=wadalite)

Figure 7. Electron microprobe maps from a quadrant of Allende Type B CAI TS34. (a) Back-scattered electron image, (b) combined elemental map constructed from Mg (red), Ca (green) and Al (blue) K_α X-rays and (c) combined elemental map constructed from Cl (red), Na (green) and Al (blue) K_α X-rays. In c), red regions correspond to wadalite, green regions correspond to nepheline, and yellow regions correspond to sodalite.

Figure 8. 200 keV brightfield transmission electron microscopy images of the wadalite-melilite interface in FIB section Wdl1. (a) Melilite is present as micron-sized laths rooted in wadalite and extending into voids. Void outlines are indicated by red curves. The direction of increasing åkermanitic content from $Åk_{\sim 25}$ to $Åk_{\sim 60}$ is indicated by an arrow. Strong zoning in the melilite suggests it may have recrystallized during fluid-mediated alteration. (b) Wadalite that co-crystallized with melilite is also present in this FIB section. Red lines indicate mineral boundaries. (c) Inclusions, probably originally filled by fluid or gas, are evident in the melilite and at melilite interfaces with wadalite. Inclusions are also present in (b). The appearance of a rim in void spaces is due to redeposition of sputtered material into the voids, an artifact of FIB sample preparation. (wdl=wadalite, mel=melilite).

Figure 9. FIB section Wdl2. (a) 300 keV high angle annular darkfield (HAADF) scanning transmission electron microscopy image of the entire section. A portion of the lower edge of the section is too thin to give much contrast in HAADF imaging. (b) 200 keV brightfield transmission electron microscopy image of submicron voids present in

grossular at the grossular-spinel interface. (C=carbon, wdl=wadalite, sp=spinel; grs=grossular, mnl=monticellite, mel=melilite, di=diopside).

Figure 10. FIB section Wdl3. (a) 300 keV high angle annular darkfield (HAADF) scanning transmission electron microscopy image of the entire section. The center portion of the section is too thin to give much contrast in HAADF imaging. (b) 200 keV brightfield transmission electron microscopy image of an apparent submicron inclusion of wadalite embayed in grossular. The wadalite grain is outlined in red. Inset is a scanning transmission electron micrograph of the same region. (C=carbon, wdl=wadalite, grs=grossular; mnl=monticellite, mel=melilite).

Figure 11. Back-scattered electron image of an outer portion of a compact Type A CAI ALH from Allende. Mellite is replaced and cross-cut by secondary anorthite. Grossular occurs at the boundary of these minerals. (grs=grossular, mel=melilite, pv=perovskite, sp=spinel).

wt %	Terrestrial wadalite	Allende CAI #, wadalite grain #		
		AJEF, Grain	AJEF, Grain	A39, Grain 3
CaO	41.4	40.8	41.5	40.8
MgO	3.1	4.9	3.3	4.2
Al_2O_3	20.9	18.3	22.1	20.5
SiO_2	19.8	24.8	20.1	22.2
Na_2O	n.d.	0.52	0.37	0.11
TiO_2	n.d.	<0.03	0.12	<0.03
FeO	2.4*	<0.06	<0.06	0.28
Cl	12.7	13.5	13.6	12.7

Table 1. Wadalite compositions from terrestrial skarns (Kanazawa et al. 1997) and from Allende CAIs AJEF and A39 obtained by electron microprobe analyses.

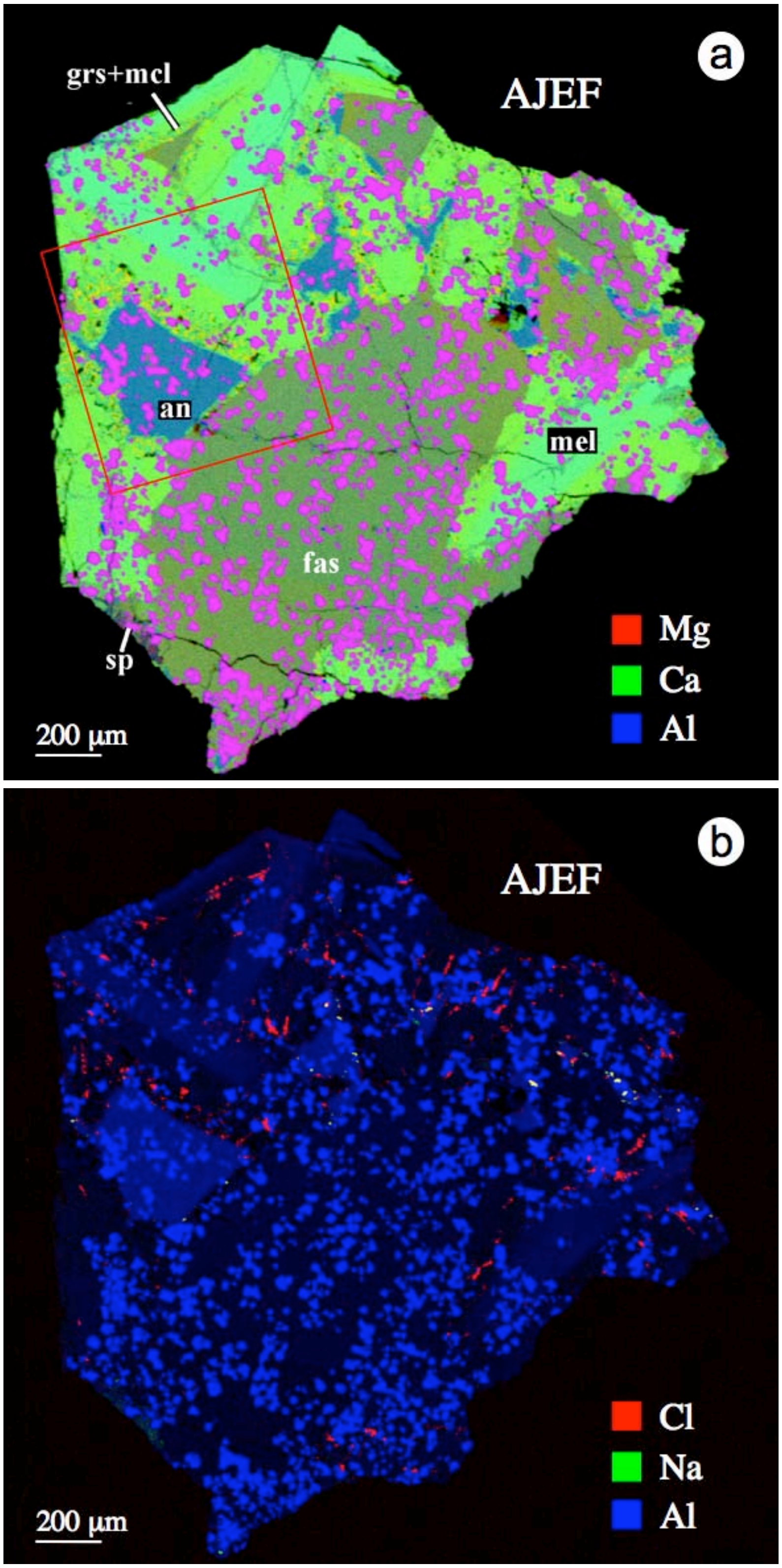

Figure 1.

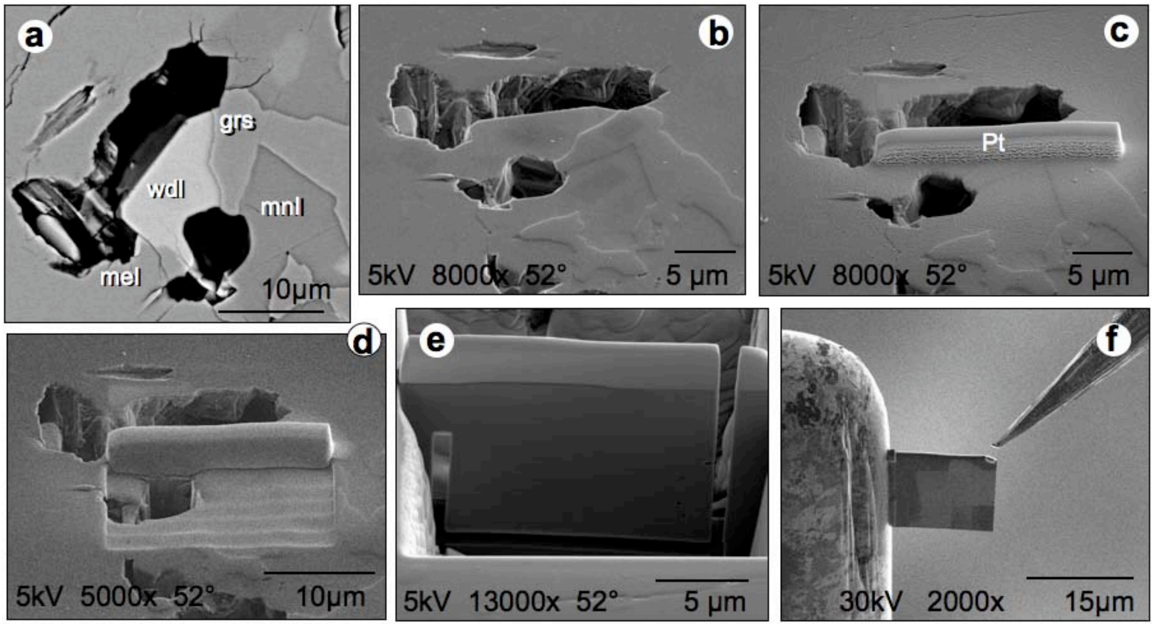
a
grs
wdl
mnl
mel
10µm
b
5kV 8000x 52°
5 µm
c
Pt
5kV 8000x 52°
5 µm
d
5kV 5000x 52°
10µm
e
5kV 13000x 52°
5 µm
f
30kV 2000x
15µm

Figure 2.

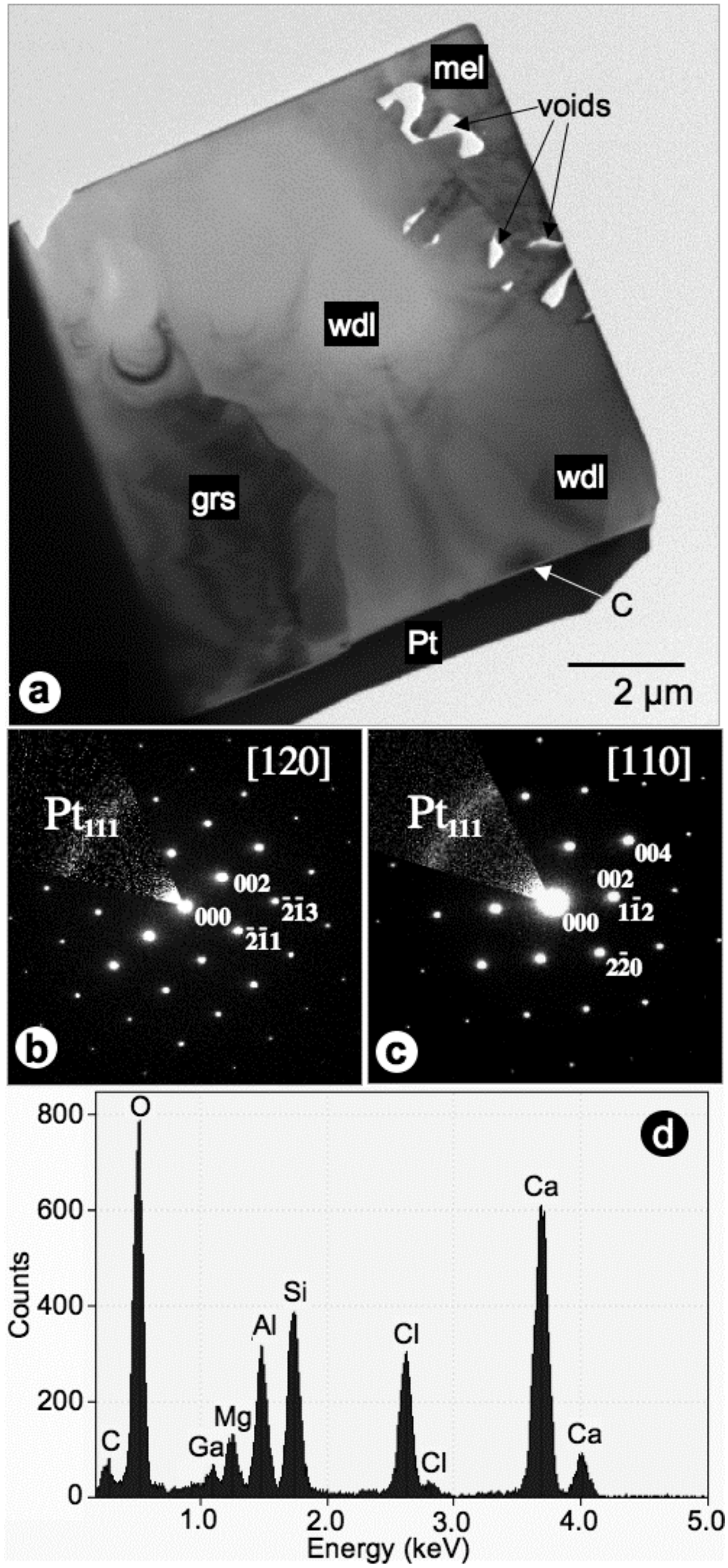

mel
voids
wdl
grs
wdl
C
Pt
a
2 μm
[120]
Pt_{111}
002
$\bar{2}\bar{1}3$
000
$\bar{2}\bar{1}1$
b
[110]
Pt_{111}
004
002
$1\bar{1}2$
000
$2\bar{2}0$
c
d
Counts
Energy (keV)
O
Ca
Si
Al
Cl
Mg
Ga
C
Cl
Ca

Figure 3.

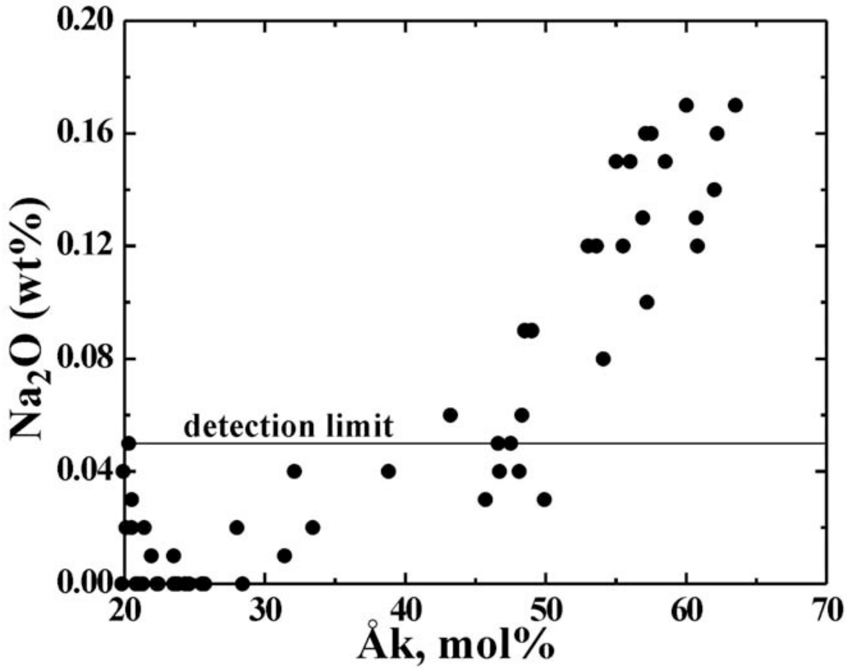

0.20
0.16
0.12
0.08
0.04
0.00
Na2O (wt%)
detection limit
20
30
40
50
60
70
Åk, mol%

Figure 4.

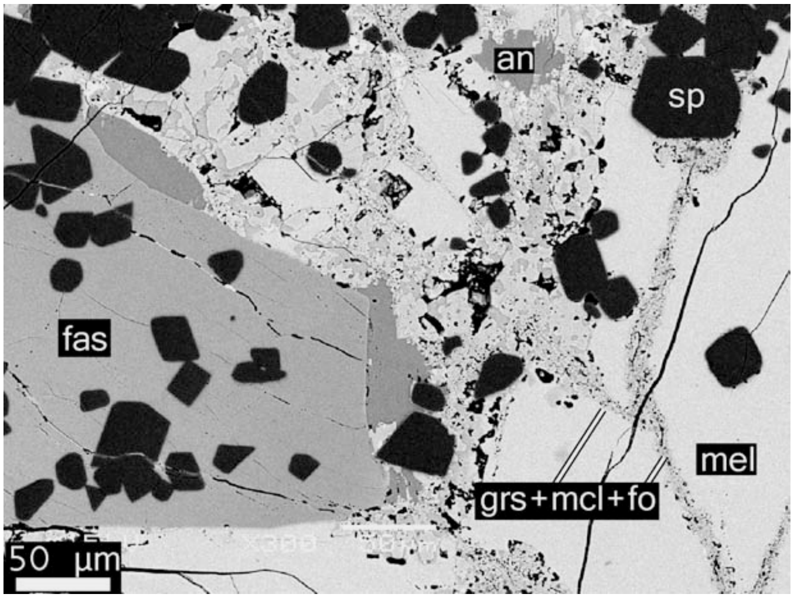

Figure 5.

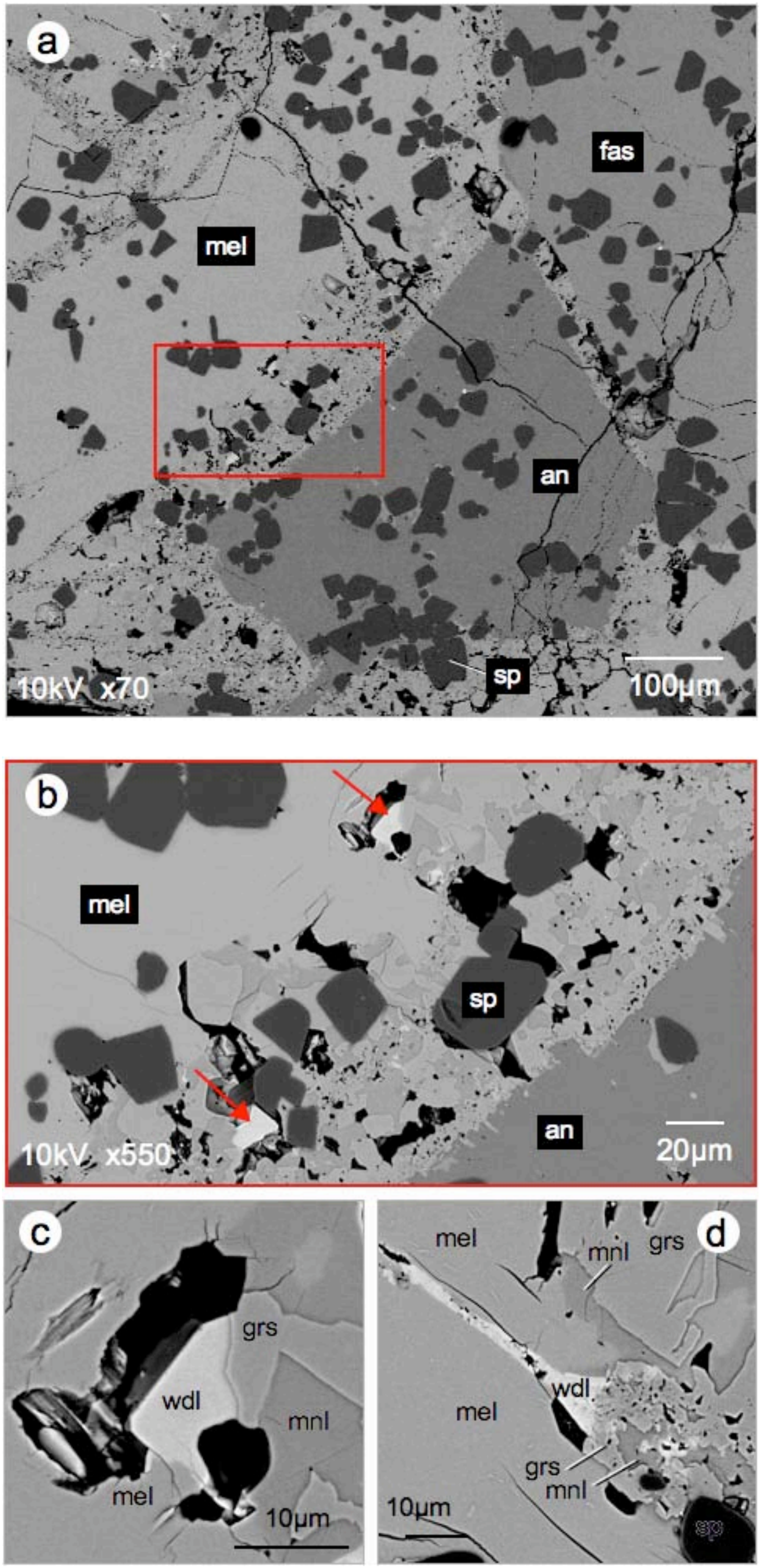
a
fas
mel
an
sp
10kV x70
100µm
b
mel
sp
an
10kV x550
20µm
c
grs
wdl
mnl
mel
10µm
mel
mnl
grs
d
wdl
mel
grs
mnl
10µm
sp

Figure 6.

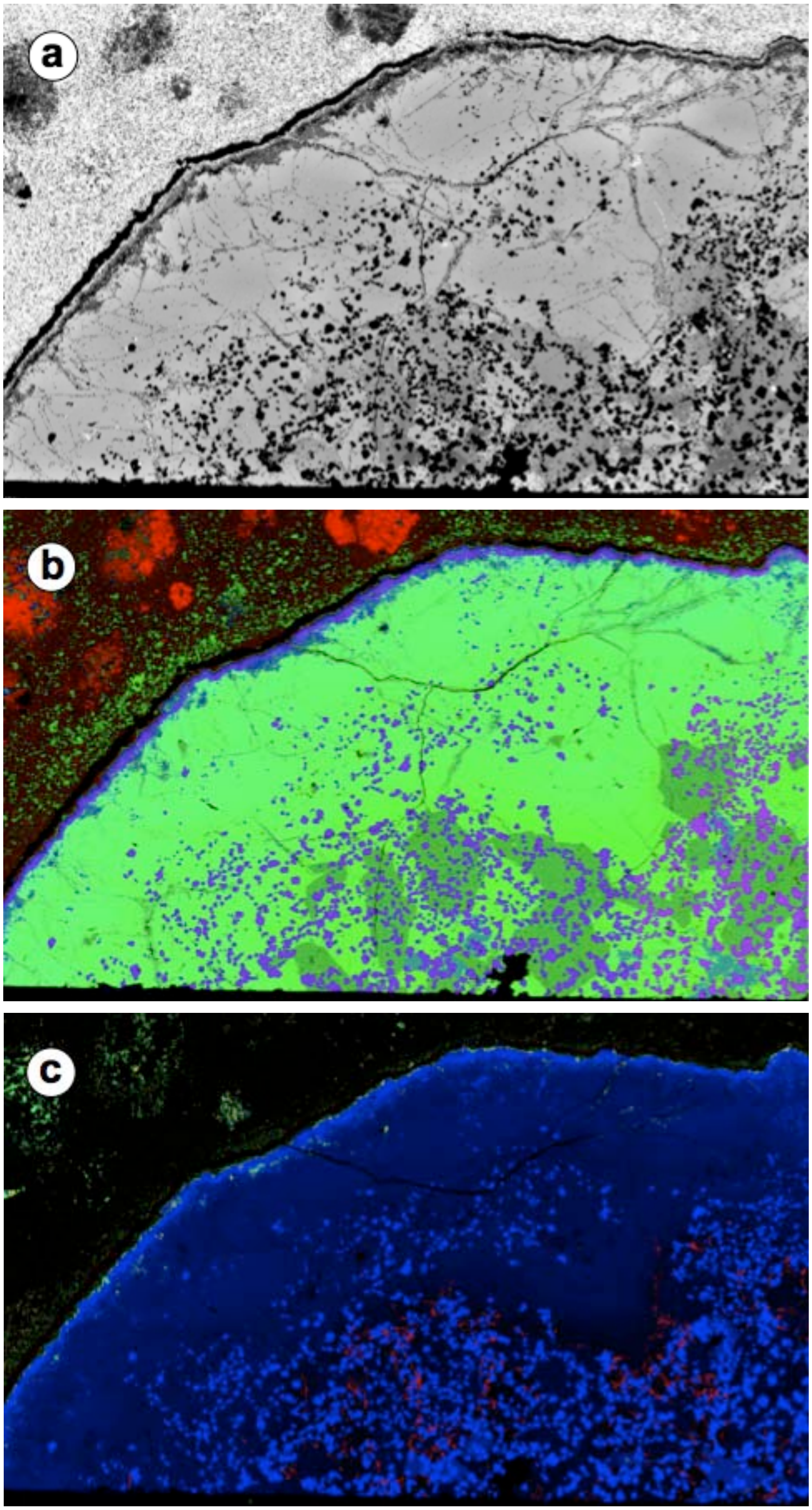

Figure 7.

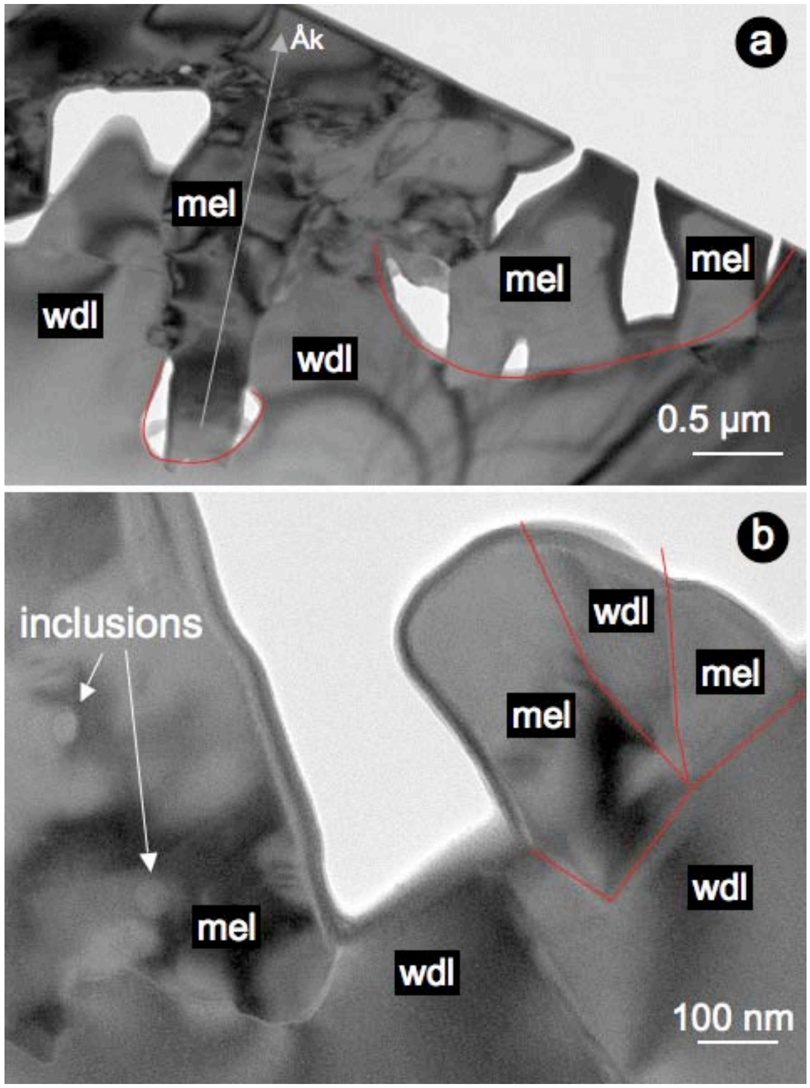
a
Åk
mel
mel
mel
wdl
wdl
0.5 µm
b
inclusions
wdl
mel
mel
mel
wdl
wdl
100 nm

Figure 8a & b

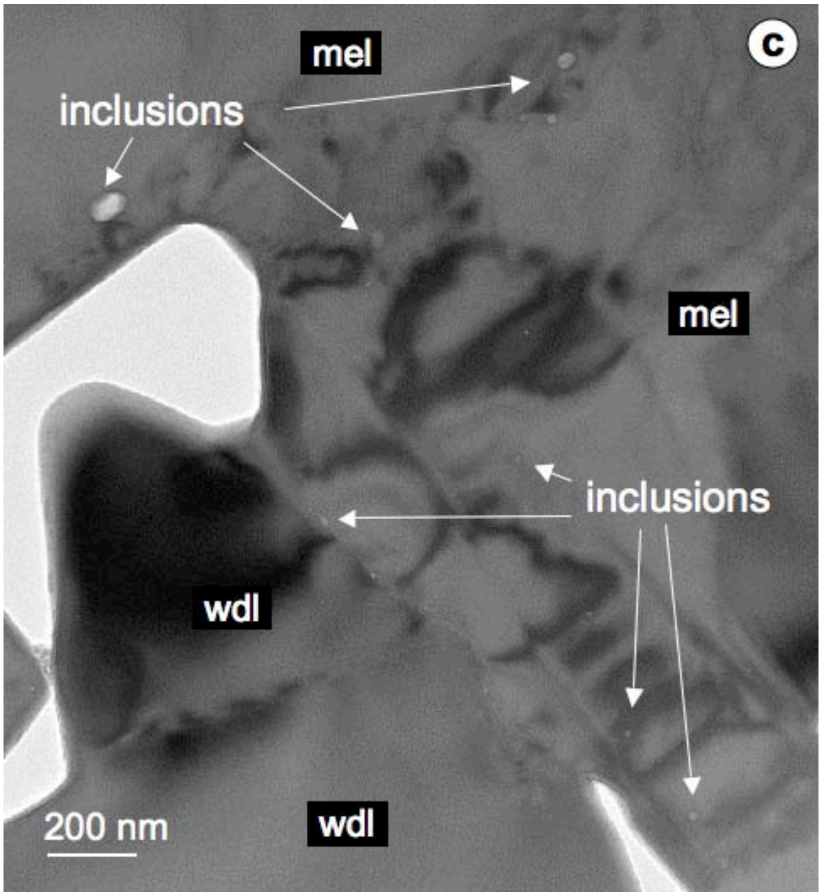

Figure 8c.

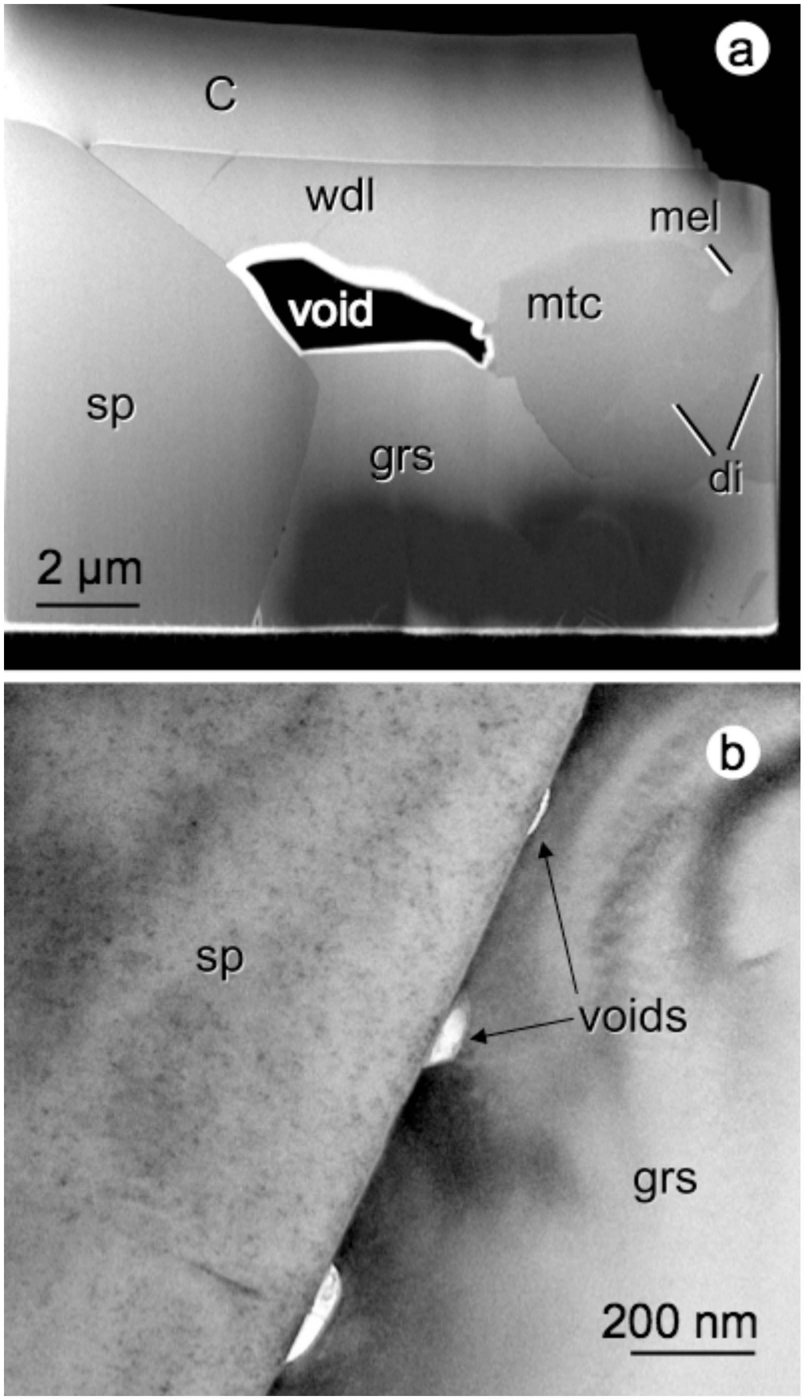

1

2 Figure 9.

3

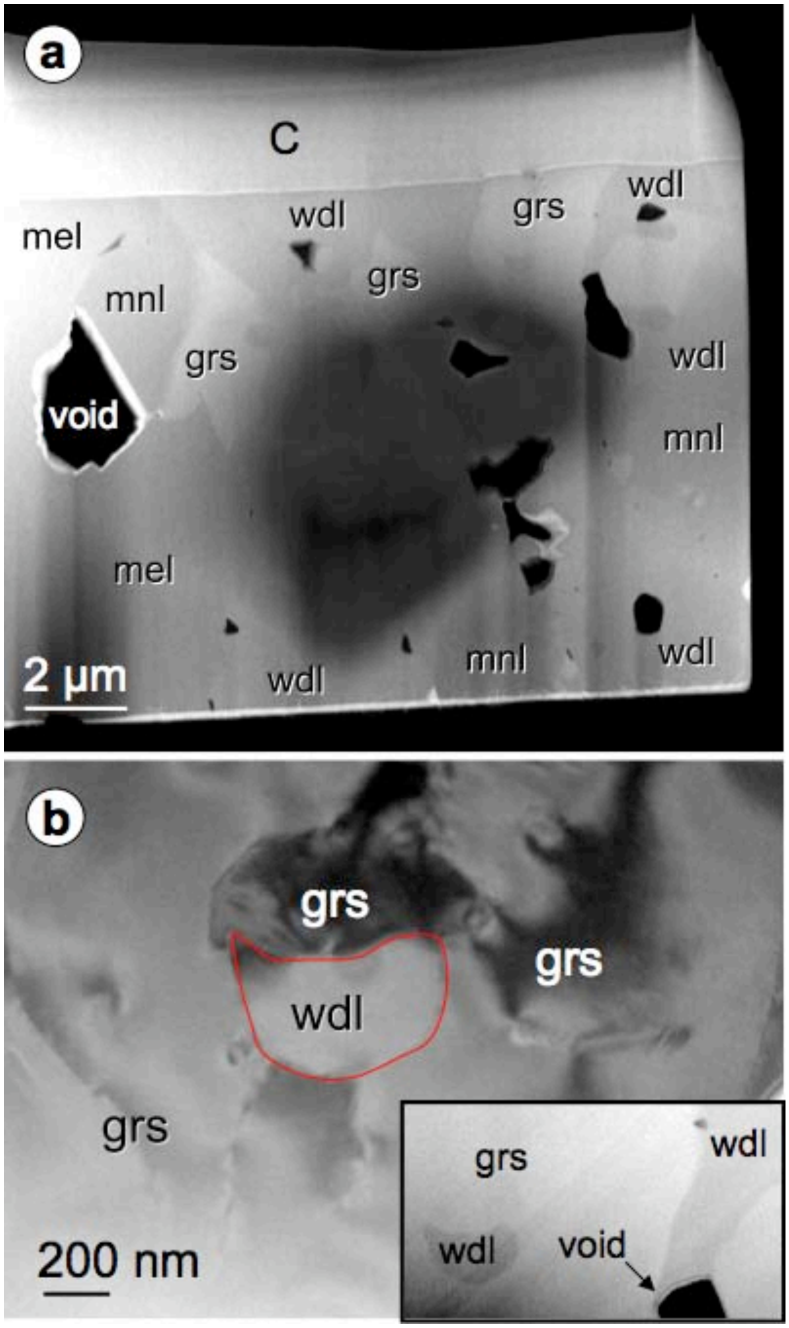
a
C
mel
wdl
grs
wdl
mnl
grs
grs
wdl
void
mnl
mel
2 µm
wdl
mnl
wdl
b
grs
grs
wdl
grs
200 nm
grs
wdl
wdl
void

Figure 10.

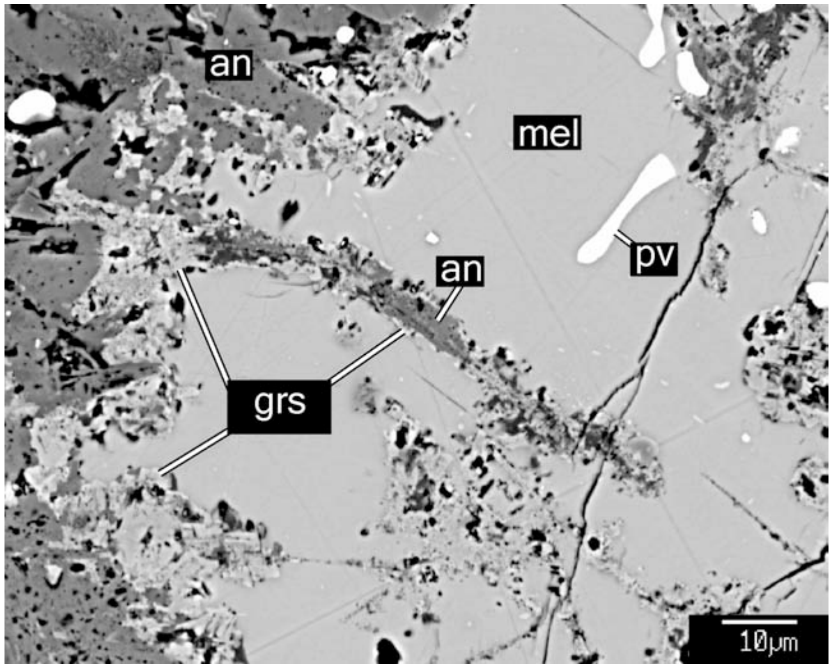

Figure 11.